

**WEIGHTED EULER CHARACTERISTIC
TRANSFORM BASED TOPOLOGICAL LOSS FOR
RECONSTRUCTING 3D IMAGES FROM SINGLE 2D
SLICES**

Kalyan Varma Nadimpalli

**Master of Technology Thesis
June 2023**



International Institute of Information Technology, Bangalore

**WEIGHTED EULER CHARACTERISTIC
TRANSFORM BASED TOPOLOGICAL LOSS FOR
RECONSTRUCTING 3D IMAGES FROM SINGLE 2D
SLICES**

**Submitted to International Institute of Information Technology,
Bangalore
in Partial Fulfillment of
the Requirements for the Award of
Master of Technology**

by

**Kalyan Varma Nadimpalli
IMT2018034**

**International Institute of Information Technology, Bangalore
June 2023**

*Dedicated to
my friends and family*

Thesis Certificate

This is to certify that the thesis titled **Weighted Euler Characteristic Transform Based Topological Loss for Reconstructing 3D Images from Single 2D Slices** submitted to the International Institute of Information Technology, Bangalore, for the award of the degree of **Master of Technology** is a bona fide record of the research work done by **Kalyan Varma Nadimpalli, IMT2018034**, under my supervision. The contents of this thesis, in full or in parts, have not been submitted to any other Institute or University for the award of any degree or diploma.

Prof. Amit Chattopadhyay



Prof. Bastian Rieck

Bengaluru,

The 14th of June, 2023.

**WEIGHTED EULER CHARACTERISTIC TRANSFORM BASED
TOPOLOGICAL LOSS FOR RECONSTRUCTING 3D IMAGES FROM
SINGLE 2D SLICES**

Abstract

The computer vision task of reconstructing 3D images, i.e., shapes, from their single 2D image slices is extremely challenging, especially in the regime of limited data. Deep learning models typically optimize geometric loss functions, which may lead to poor reconstructions as they ignore the structural properties of the shape. To tackle this, we propose a novel topological loss function based on the Weighted Euler Characteristic Transform which is both computationally efficient and expressive. This loss acts as an additional inductive bias to aid the optimization of any neural network toward better reconstructions in the regime of limited data. We show the effectiveness of the proposed loss function by incorporating it into SHAPR, a state-of-the-art shape reconstruction model, and test it on a benchmark dataset, viz., Red Blood Cells dataset. We also discuss injectivity results and prove the stability of the Euler Characteristic Transform.

Acknowledgements

I would like to express my sincerest gratitude to a long list of individuals who are responsible for making this thesis a reality. First and foremost, I profoundly acknowledge the unwavering patience and moral support shown by my parents. Furthermore, the timely advice and invaluable guidance from my supervisors – Prof. Amit Chattopadhyay and Prof. Bastian Rieck (Professor at Helmholtz Munich) – played a pivotal role in successful completion of this thesis. Finally, a hearty thanks to IIT-Bangalore for providing me with a rich learning atmosphere and strong theoretical fundamentals which were crucial for this thesis.

List of Publications

1. Nadimpalli, Kalyan Varma, Amit Chattopadhyay, and Bastian Rieck. "Euler Characteristic Transform Based Topological Loss for Reconstructing 3D Images from Single 2D Slices." TAG-PRA (Topology, Geometry, Algebra in Pattern Recognition with Applications), A Workshop at the IEEE Computer Vision and Pattern Recognition (IEEE CVPR) in Vancouver, Canada, June 18th, 2023.

Contents

Abstract	iv
Acknowledgements	v
List of Publications	vi
List of Figures	x
List of Tables	xi
List of Abbreviations	xii
1 Introduction	1
1.1 Introduction	1
2 Background	3
2.1 Prior Work	3
2.2 Mathematical Background	4
2.2.1 Simplicial and Cubical Complex	5

2.2.2	Sublevel Sets and Filtrations	6
2.2.3	Euler Characteristic Curve	7
2.2.4	Weighted Euler Curve	8
2.2.5	Euler Characteristic Transform	8
2.2.6	Weighted Euler Characteristic Transform	9
2.2.7	Distance between ECTs	9
3	Our Method: Weighted Euler Characteristic Transform-based Loss	10
3.1	Overview	10
3.2	WECT Based Training Algorithm	11
3.3	WECT Computation	13
3.4	Note on V and E-Construction	14
4	Theoretical Results	16
4.1	Theoretical Properties	16
4.1.1	Injectivity Property	16
4.1.2	A Discussion on Stability of ECT-Based Loss	16
5	Experimental Results	21
5.1	Experimental Results	21
6	Conclusion and Future Work	24

Bibliography

List of Figures

FC2.1	Examples of cubical complex construction from binary images. (b) and (d) are the cubical complexes corresponding to the binary images (a) and (c), respectively.	6
FC3.1	Workflow of our proposed method. [1] Given a 2D image, a neural network produces a 3D output. The neural network is then trained on the sum of a geometric loss function like DICE loss or BCE and our proposed topological loss function, the distance between the WECTs of the images. Neural network image generated from [2].	11
FC5.1	Qualitative results on the RBC dataset. The WECT result is significantly better than the others	23
FC5.2	Qualitative results on the RBC dataset. Both the topology losses don't have artifacts unlike the SHAPR baseline	23

List of Tables

TC5.1 Performance of different variants of the SHAPR model on the Red blood cells dataset with the best performing algorithm highlighted in bold	22
---	----

List of Abbreviations

2D	2 Dimensional
3D	3 Dimensional
Card	Cardinality
CV	Computer Vision
Dim	Dimension
ECT	Euler Characteristic Transform
EC	Euler Curve
IITB	International Institute of Information Technology Bangalore
ML	Machine Learning
RBC	Red Blood Cells
TDA	Topological Data Analysis
WEC	Weighted Euler Curve
WECT	Weighted Euler Characteristic Transform

CHAPTER 1

INTRODUCTION

1.1 Introduction

Our brains possess the amazing ability to be able to reconstruct 3D shapes from single 2D images by leveraging prior knowledge and inductive biases about the shapes and sizes of objects based on the information captured from previously observed objects [3]. However, for a computer this inverse problem is ill-posed and extremely challenging. This is because for a single 2D image the space of possible 3D reconstructions is very large and often ambiguous.

There have been prior deep learning-based attempts to solve this challenge, but most of them rely on large datasets and/or 3D models of the shape [4–6]. The biomedical setting in which we consider this problem, unfortunately, does not provide large labeled datasets and it is too expensive to construct them. The sizes of the datasets available in the biomedical domain are orders of magnitude smaller than the ones available in other domains. To this end, we focus on improving reconstruction performance not by using 3D models or large datasets but instead by adding additional inductive biases in the form of a topology-based regularization to the optimization process. Most models typically optimize geometry-based loss functions that work on a per-pixel basis, such as the DICE loss. We improve the performance of an existing neural network by adding a novel

complementary topology-based loss that considers more global topological features, such as connectivity, tunnels, or voids. Specifically, we design a novel regularization term based on the Weighted Euler Characteristic Transform [7], that is computationally efficient, can work with any image size and can be plugged into any neural network. An overview of how our loss function can be used can be seen in Figure FC3.1. We demonstrate the efficacy of the proposed loss function by plugging it into the SHAPR model and testing it on two bio-medical datasets used in the prior work [8,9]. In the current paper, our key contributions are as follows:

- We adapt the Weighted Euler Characteristic Transform (ECT), obtaining a novel topological loss function for 3D shape reconstruction that is compatible with any neural network architecture.
- We discuss injectivity results of the ECT and WECT as well as prove stability results of ECT and WECT on binary images.
- We show the effectiveness of the proposed method by training the SHAPR model [8] with our proposed loss on the RBC dataset.

Outline. In Chapter 2 we go over the literature relevant to our work as well as the mathematical background required to understand our topological loss. Subsequently, in Chapter 3 we describe our proposed loss functions in detail as well as how they fit into the overall training of a neural network. In Chapter 4 we then prove and discuss favourable mathematical properties of the WECT. Finally in Chapter 5 we then demonstrate the efficacy of our model and discuss the significance of our results. Finally in Chapter 6 we summarize our work and list some potential future work.

CHAPTER 2

BACKGROUND

2.1 Prior Work

Multiple variants of the problem of 2D to 3D image reconstruction have been studied by various communities for different applications like scene understanding, medical, robot navigation, etc. [3]. The tasks considered differ in their input type, some variants consider multiple slices as the input while some consider a single image like in our formulation. Among the models that only take a single image as an input, most of them require a synthetic 3D model of the output or very large datasets [4–6].

The application of computational topology to machine learning is an emerging field that has shown promise in various applications [10]. It has recently been used extensively in computer vision tasks like segmentation, image generation, etc. [11–13]. In the current paper, we improve the performance of image reconstruction models using tools from topology, namely, the Euler Characteristic Transform [7].

SHAPR [8] is the first machine learning model that considers the problem of 2D to 3D reconstruction in the case of biomedical images. This model proved to be significantly better than standard synthetic models like a cylindrical fit and ellipsoid fit. They also showed that features extracted from the 3D reconstruction helped to improve accuracy in downstream classification tasks on the 2D images. Recently, a diffusion-

based model DISPR [14] has been introduced that outperforms the GAN-based SHAPR model.

Waibel et al. [9] extend the SHAPR model by training the model on a combined loss function of both the DICE loss as well as a regularization term defined by the Wasserstein distance between the persistence diagrams—topological descriptors—of the predicted shape and the ground truth. This model outperforms the SHAPR model and provides much better reconstructions than the vanilla SHAPR model. However, it has been shown by Oner et al. [12] that such persistence diagram based loss functions are not optimal for the following reasons:

- Since the ground truth images are binary images, calculating the persistence diagrams over the filtration of pixel values degenerates to calculating the Betti numbers, which is a topological measure of limited expressivity.
- Persistence diagrams throw away location information and are generally not injective mappings, thus potentially leading to erroneous matchings, which in turn may lead to wrong reconstructions.

To overcome these drawbacks, we develop a novel topological loss based on the WECT.

2.2 Mathematical Background

In this section, we briefly introduce the mathematical background required for our work, for a more detailed explanation we refer the reader to Edelsbrunner et al. and Turner et al. [7, 15].

2.2.1 Simplicial and Cubical Complex

A simplicial complex is the fundamental building block of algebraic topology, comprised of simplices. A k -simplex σ can be understood as the convex hull of $k + 1$ affinely independent points. A 0-simplex is a point, a 1-simplex is an edge, a 2-simplex is a triangle and a 3-simplex is a tetrahedron. A face τ of a simplex is the convex hull of a subset of the $k + 1$ points. It is often represented as a face by the notation $\tau \preceq \sigma$. A simplicial complex K is a finite collection of simplices satisfying two conditions:

1. $\sigma \in K$ and $\tau \preceq \sigma$ implies that $\tau \in K$
2. $\sigma, \sigma_0 \in K$ implies $\sigma \cap \sigma_0$ is either empty or a face of both.

The dimension of the simplicial complex is the dimension of the largest simplex in the complex, denoted by $\text{Dim}(K)$. A subcomplex L is a subset of a simplicial complex K . K^d is a particular subcomplex that is defined as a subcomplex consisting of all simplices of dimension d from K , that is, $K^d = \{\sigma \in K \mid \dim(\sigma) = d\}$.

A cubical complex is a special variant of a simplicial complex that is particularly useful in representing grid-like shapes. It has recently caught traction in applications for image processing due to the fact that it is better aligned to the grid-like structure of images [16, 17]. Informally, a cubical complex is identical to a simplicial complex except that n -simplices are replaced with n -cubes. For example, the triangles (2-simplices) are replaced by squares (2-cubes), and tetrahedra (3-simplices) by cubes (3-cubes) and so on. Note that all definitions in this section hold for both simplicial and cubical complexes.

We define a weighted cubical complex to be one with an associated scalar function $f : K \rightarrow \mathbb{R}$. This weighted cubical complex can be used to compute weighted euler characteristic and other such invariants defined later in this section.

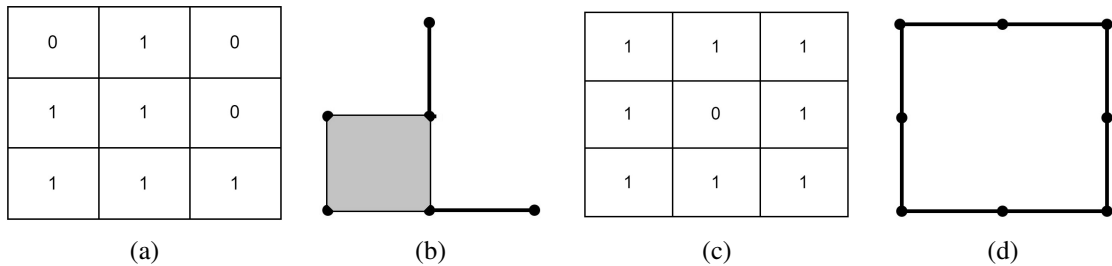


Figure FC2.1: Examples of cubical complex construction from binary images. (b) and (d) are the cubical complexes corresponding to the binary images (a) and (c), respectively.

Given a d -dimensional image with a scalar function defined on the voxels, we present two ways to convert it to a weighted cubical complex. The first step common to both of them is to convert it to a cubical complex by defining the 0-cubes as the set of voxels. Then an i -dimensional cube is formed by connecting a set of 2^i adjacent voxels whose voxel values are positive. Note that two d -dimensional voxels are adjacent if they share a $(d - 1)$ -dimensional face. Thus 1-cubes are the edges corresponding to two adjacent voxels with values 1. Similarly, the 2-cubes are the squares corresponding to four adjacent voxels with positive values and so on. Two examples of this construction can be seen in Figure FC2.1. Now, our scalar function is only defined on the voxels, there are two ways to extend this to hyper-dimensional cubes:

1. V-Construction: This is a method used commonly in TDA literature, where the value of higher dimensional cubes is the value of the max of it's faces.
2. E-Construction: This is a method we propose for our special case where we define the value of higher dimensional cubes as the product of it's constituent vertices. The benefits of which will be discussed at the end of chapter 3.

2.2.2 Sublevel Sets and Filtrations

Consider a simplicial or cubical complex K and a monotonic function $f : K \rightarrow \mathbb{R}$. By f being monotonic, we mean $f(\sigma) \leq f(\tau)$ whenever $\sigma \preceq \tau$. For such monotonic

functions, the sublevel set $K(a)$ corresponding to a real value a is defined by

$$K(a) = f^{-1}(-\infty, a],$$

which is a subcomplex of K . If there are m simplices in K , as we increase a , we get $r + 1 \leq m + 1$ different subcomplexes which can be arranged in an increasing sequence,

$$\emptyset = K_0 \subseteq K_1 \dots \subseteq K_r = K$$

where $K_i = K(a_i)$ and $a_1 < a_2 < \dots < a_r$ are the distinct function values of f at the simplices of the simplicial complex K . This sequence of complexes is called the filtration of K with respect to f . A common filtration we consider is the height filtration. Given a height h and a particular direction \vec{u} , we define the sub-complex $K_{\vec{u},h}$ consists of all the simplices of K whose vertices have height $\leq h$ along the direction \vec{u} . We can naturally define a filtration by increasing the value of h along the direction \vec{u} .

2.2.3 Euler Characteristic Curve

Given a d -dimensional simplicial complex K , the Euler Characteristic Curve of K along a direction \vec{u} is a function $EC_{\vec{u},K} : \mathbb{R} \rightarrow \mathbb{Z}$ defined by

$$h \mapsto \chi(K_{\vec{u},h}), \tag{Eqn 2.1}$$

where $\chi(K_{\vec{u},h})$ is the Euler characteristic of the simplicial complex $K_{\vec{u},h}$, which is defined as

$$\chi(K_{\vec{u},h}) = \sum_{i=0}^d (-1)^i \text{Card } K_{\vec{u},h}^i, \tag{Eqn 2.2}$$

where $\text{Card}(K_{\vec{u},h}^i)$ denotes the number of i -simplices in the subcomplex $K_{\vec{u},h}^i$. By computing the Euler characteristic alongside a filtration, we obtain the *Euler Characteristic Curve*. This construction works for general filtrations and is not restricted to the height

filtration.

2.2.4 Weighted Euler Curve

Given a d -dimensional simplicial complex K with an associated weight function defined on the vertices $w : V \rightarrow \mathbb{R}$, Jiang et al. [18] define the weighted Euler characteristic of K as:

$$\kappa'(K) = \sum_{i=0}^d (-1)^i \sum_{\sigma \in K^i} w(\sigma). \quad (\text{Eqn 2.3})$$

where V is the set of vertices of K . The value of w for a simplex is the maximum of its values at the constituent vertices, i.e., for an i -simplex $\sigma = \langle v_0, v_1, \dots, v_i \rangle$,

$$w(\sigma) = \max\{w(v_0), \dots, w(v_i)\}.$$

The weighted Euler curve can be defined similarly as the Euler curve, by replacing the Euler characteristic with the weighted Euler characteristic. Thus, given a simplicial complex K , the weighted Euler curve of K along the direction \vec{u} is a function $\text{WEC}_{\vec{u}, K} : \mathbb{R} \rightarrow \mathbb{R}$ which is defined mathematically as:

$$h \rightarrow \kappa'(K_{\vec{u}, h}).$$

where $\kappa'(K)$ is the weighted Euler characteristic of the simplicial complex K .

2.2.5 Euler Characteristic Transform

The Euler Characteristic Transform (ECT) [7] of a d -dimensional simplicial complex K , denoted by $\text{ECT}_K : \mathbb{S}^{d-1} \rightarrow \mathbb{Z}^{\mathbb{R}}$, is defined by

$$\vec{v} \rightarrow \text{EC}_{\vec{v}, K}, \quad (\text{Eqn 2.4})$$

where the direction \vec{v} is chosen from the $(d-1)$ -dimensional unit sphere \mathbb{S}^{d-1} . That is, the ECT is the set of all Euler Characteristic Curves obtained over the height filtrations along all possible directions.

2.2.6 Weighted Euler Characteristic Transform

The Weighted Euler Characteristic Transform (WECT) [18] of K , denoted by $WECT_K : \mathbb{S}^{d-1} \rightarrow \mathbb{R}^{\mathbb{R}}$, is defined as:

$$\vec{v} \rightarrow WEC_{\vec{v},K}.$$

Analogous to the ECT, it is the set of Weighted Euler Curves obtained over the height filtrations of all possible directions chosen from the $(d-1)$ -dimensional unit sphere \mathbb{S}^{d-1} . The WECT is the heart of our method. We use it as a topological descriptor to capture the important topological features of 3D images to define our topological loss functions.

2.2.7 Distance between ECTs

The distance between two ECTs corresponding to two complexes K_1 and K_2 is defined by

$$d(\text{ECT}_{K_1}, \text{ECT}_{K_2}) = \int_{\vec{u} \in \mathbb{S}^{d-1}} \|\text{EC}_{\vec{u},K_1} - \text{EC}_{\vec{u},K_2}\|^2 d\mu, \quad (\text{Eqn 2.5})$$

where $\|\cdot\|$ is the l_2 -norm. We use this distance to compute the topology based loss function to train our neural network. In practice, the integration in equation (Eqn 2.5) is computed using the Monte Carlo method, i.e., we compute the average of the l_2 -norms between the Euler curves along a finite number randomly sampled directions from \mathbb{S}^{d-1} . Analogously we define the distance between two WECTs replacing the above definition with WEC instead of EC.

CHAPTER 3

OUR METHOD: WEIGHTED EULER CHARACTERISTIC TRANSFORM-BASED LOSS

In this chapter, first we describe the overall workflow of our 3D image reconstruction method and how our loss function fits into a neural network training procedure (subsection 3.1). Subsequently, we give the detailed algorithms to compute the proposed loss functions (subsections 3.2, 3.3, algorithms 1, 2, 3).

3.1 Overview

In our method, we develop a loss function based on the WECT to train a neural network for 3D image reconstruction from a single 2D slice. Figure FC3.1 shows the workflow of our model, which is explained in the following steps.

1. Given a 2D slice, it is first passed through a neural network that gives an output 3D image I , where for each voxel x of I , the model assigns the likelihood of x being part of the true 3D image.
2. Given the 3D prediction I and the 3D ground truth Y , we use the DICE loss combined with a scaled WECT-based loss function, denoted L_{TL} , to optimize the neural network.

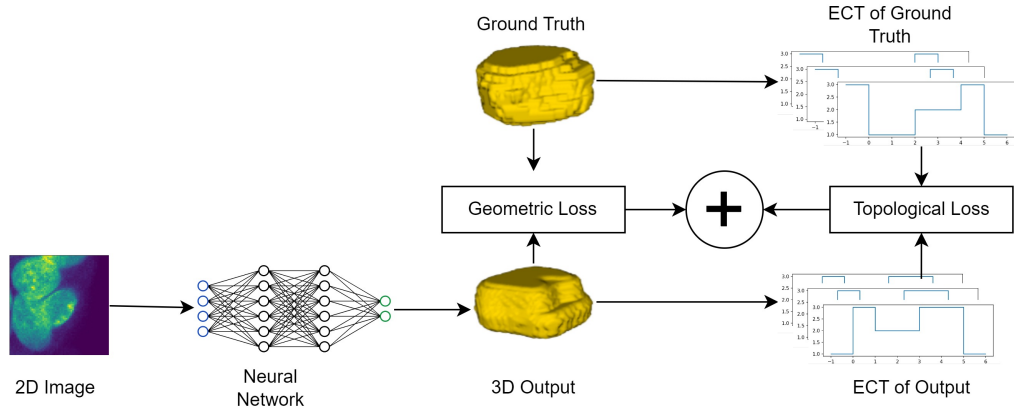


Figure FC3.1: Workflow of our proposed method. [1] Given a 2D image, a neural network produces a 3D output. The neural network is then trained on the sum of a geometric loss function like DICE loss or BCE and our proposed topological loss function, the distance between the WECTs of the images. Neural network image generated from [2].

Mathematically, this can be represented as:

$$L(I, Y) = L_{DICE}(I, Y) + \lambda L_{TL}(I, Y), \quad (\text{Eqn 3.1})$$

where λ is the weight parameter for the topological loss term.

This is a similar setup as described by Waibel et al. [9], however, our method differs in the details of the topology-based loss $L_{TL}(I, Y)$ and as a result the efficacy of it as well. Next, we discuss our Algorithm 1 to train a neural network by computing the topological loss terms based on WECT, in detail.

3.2 WECT Based Training Algorithm

Given a dataset of 2D slices and corresponding 3D images, we first train the SHAPR model based on the proposed WECT-based loss function.

Algorithm 1 TRAINSHAPRMODELBASEDONECT

Input: X - 2D image slice,

 Y - Corresponding 3D ground-truth image,

 t - Number of thresholds,

 Θ_0 - Initial model parameters

Output: Trained SHAPR Model

```

1:  $\Theta \leftarrow \Theta_0$  % Initialize model parameters

2: for epoch = 1, 2, ..., N do
3:    $I \leftarrow \text{SHAPR}(X, \Theta)$ 
4:    $L_{\text{Topo}} \leftarrow 0$  % Initialize the Topology Loss

5:   % Compute WECT-based Topological Loss
6:    $A \leftarrow \text{E-Construction}(I)$ 
7:    $B \leftarrow \text{E-Construction}(Y)$ 
8:   Sample  $l$  directions  $\{\vec{u}_1, \vec{u}_2, \dots, \vec{u}_l\}$  from  $\mathbb{S}^2$ 
9:    $\text{WECT}_A \leftarrow \text{ComputeWECT}(A, \{\vec{u}_1, \vec{u}_2, \dots, \vec{u}_l\})$ 
10:   $\text{WECT}_B \leftarrow \text{ComputeWECT}(B, \{\vec{u}_1, \vec{u}_2, \dots, \vec{u}_l\})$ 
11:   $L_{\text{Topo}} += (\text{WECT}_A - \text{WECT}_B)^2$ 
12:  % Compute Total Loss
13:   $L = L_{\text{DICE}} + \lambda L_{\text{Topo}}$ 

14:  % Perform Gradient Update Step to Update the Model Parameters  $\Theta$  with Learning Rate
       $\alpha$ 
15:   $\Theta \leftarrow \Theta - \alpha \nabla_{\Theta} L$ 

16: end for

```

For ease of understanding, in Algorithm 1, we demonstrate the training of the SHAPR model on a single training sample, i.e., using a 2D slice image X and its ground-truth 3D image Y . In every epoch (or training step), the image X is first passed to the SHAPR model and an output 3D image I is produced by the model (Line 3). Then at each step, we compute the WECT-based

loss function using Monte Carlo sampling. Towards this we first convert the image to a cubical complex using either the V or E construction. Next we calculate the corresponding WECTs from the respective cubical complexes. Finally, the topological loss function is computed using the average of l_2 -norms between $WECT_A$ and $WECT_B$. A scaled version of this topological loss (here, λ is the scaling factor) is added with the standard DICE loss to compute the total loss (Line 18). The model parameters Θ are then updated by optimizing this loss using a gradient descent method (Line 19).

3.3 WECT Computation

In this sub-section, we explain the details of approximating the WECT for an image A using l sampled directions $\{\vec{u}_1, \vec{u}_2, \dots, \vec{u}_l\}$ from \mathbb{S}^2 whose pseudocode is given in Algorithm 2. Broadly, we first construct a cubical complex C from the binary image A using the method explained in Section 2.2.1 (Line 1, Algorithm 2). Then for each sampled direction \vec{u}_i we compute the Weighted Euler Curve of C along the direction \vec{u}_i (Lines 4-6). The obtained set of l Weighted Euler Curves is returned as our Weighted Euler Characteristic Transform (Line 7).

Algorithm 2 COMPUTEWECT

Input: A - 3D Binary Image, l sampled directions $\{\vec{u}_1, \vec{u}_2, \dots, \vec{u}_l\}$ from the unit sphere \mathbb{S}^2

Output: ECT_A

```

1:  $C \leftarrow \text{CubicalComplex}(A)$ 
2:  $ECT_A \leftarrow []$  % Initialize as an empty array
3: % Compute Weighted Euler curves along the  $l$  directions
4: for  $i = 1, 2, \dots, l$  do
5:    $ECT_A.add(\text{WeightedEulerCurve}(C, \vec{u}_i))$ 
6: end for
7: return  $ECT_A$ 

```

The Weighted Euler Curve computation of a cubical complex C along a sampled direction \vec{u} is described in Algorithm 3. We compute the minimum h_{min} and maximum h_{max} of all heights of the vertices $\mathbf{v}_0, \mathbf{v}_1, \dots, \mathbf{v}_n$ in the cubical complex C along the direction \vec{u} (Lines 1-2). For a chosen parameter M , we sample the height field at $M + 1$ equally spaced heights of step-size dh (Line 5). For each sampled height, we calculate the Weighted Euler Characteristic κ' of the sub-complex $C_{\vec{u},h}$ (Lines 7-10). We return the list of obtained values as our discrete representation of the Weighted Euler curve. Note that the smaller the step size dh , the closer our representation is to the continuous Weighted Euler Curve.

Algorithm 3 WEIGHTEDEULERCURVE

Input: C - Cubical complex , \vec{u} - Direction vector

Output: $EC_{u,C}$

```

1:  $h_{min} \leftarrow \min(\vec{u} \cdot \mathbf{v}_0, \dots, \vec{u} \cdot \mathbf{v}_n)$ 
2:  $h_{max} \leftarrow \max(\vec{u} \cdot \mathbf{v}_0, \dots, \vec{u} \cdot \mathbf{v}_n)$ 
3:  $WEC_{u,C} = []$  %Initialize as an empty array
4:  $h \leftarrow h_{min}$ 
5:  $dh = (h_{max} - h_{min})/M$  % Step length with parameter M
6: % Compute Weighted Euler curve of M + 1 steps
7: while  $h \leq h_{max}$  do
8:    $WEC_{u,C}.add(\kappa'(C_{\vec{u},h}))$ 
9:    $h += dh$ 
10: end while
11: return  $WEC_{u,C}$ 

```

3.4 Note on V and E-Construction

In our specific case the voxels all have a value between 0 and 1 representing the likelihood of the voxel. We define the E-construction in the way we do so that the value of a higher

dimensional cube is equivalent to the likelihood that it exists. This way the Weighted Euler number that we calculate is actually the expected Euler number of the complex. So our loss reduces to minimizing the distance between the expected ECTs of the ground truth and the prediction.

CHAPTER 4

THEORETICAL RESULTS

4.1 Theoretical Properties

In this section, we analyze and prove some important properties of the transform and the proposed loss function to evaluate our method.

4.1.1 Injectivity Property

Turner et al. [7] have shown that ECT over the space of simplicial complexes in \mathbb{R}^3 is injective. Subsequently, Curry et al. [19] has shown that picking a finite few careful directions leads to an injective transform. Jiang et al. [18] show that the WECT is an injective transform.

4.1.2 A Discussion on Stability of ECT-Based Loss

A commonly studied property in computational topology is the stability of a transform, that is the effect of perturbations on the input to the transformed output [20,21]. We discuss a similar property for the case of ECT on binary images. We bound the possible change in the ECT of a binary image by a constant proportional to the size of the image and the size of the change in the input. We first prove a necessary lemma for our proof in Lemma 1. We then show that the distance between two EC's is bounded in Theorems 2 and 3. Subsequently we prove that the

ECT is bounded in Corollary 1. We then discuss the effect of thresholding on stability.

Lemma 1. *A vertex in a d -dimensional grid is a part of at most 3^d cubes of any dimension.*

Proof. Consider a vertex $\mathbf{v}_0 = (x_1, x_2, \dots, x_d)$ in the interior of the grid. Every k -cube, that has \mathbf{v}_0 as a vertex, can be uniquely determined by k adjacent vertices of \mathbf{v}_0 along different dimensions in the grid. Along the i -th dimension \mathbf{v}_0 has two adjacent vertices $(x_1, x_2, \dots, x_i \pm 1, \dots, x_d)$, along positive and negative directions.

Now to count the number of k -cubes, that \mathbf{v}_0 is a part of, we simply count the number of ways we can choose k possible directions from the total d directions, which is $\binom{d}{k}$. Then for each of these chosen directions, we can either choose the adjacent vertices along the positive or negative direction, i.e in 2^k ways. So the total number of k -cubes, that \mathbf{v}_0 is a part of, is $2^k \binom{d}{k}$. Summing up over all dimensions we get:

$$\sum_{k=0}^d \binom{d}{k} 2^k = 3^d.$$

Note that we performed the calculation for an interior vertex. For the vertices on the boundary of the grid, each will be a part of fewer cubes. So we can bound the number of cubes, that a single vertex is a part of, by 3^d . ■

Theorem 2. *Let I and I^* be two d -dimensional binary images with vertex set V s.t. they differ only at one voxel. Then along an arbitrary direction \vec{u} ,*

$$D(\text{EC}_{\vec{u}, I}, \text{EC}_{\vec{u}, I^*}) \leq 3^d n / \sqrt{d}$$

where $n = |V|$ and $D(\text{EC}_{\vec{u}, I}, \text{EC}_{\vec{u}, I^*})$ is the l_2 -norm between $\text{EC}_{\vec{u}, I}$ and $\text{EC}_{\vec{u}, I^*}$, i.e.

$$D(\text{EC}_{\vec{u}, I}, \text{EC}_{\vec{u}, I^*}) = \sqrt{\int_{h_{\min}}^{h_{\max}} (\chi(C_{\vec{u}, h}) - \chi(C_{\vec{u}, h}^*))^2 dh.}$$

Proof. Let C be the cubical complex with vertices $\mathbf{v}_1, \mathbf{v}_2, \dots, \mathbf{v}_n$ associated with image I , using

the construction described in Section 2.2.1. Let $h_1 \leq h_2 \leq \dots \leq h_n$ be the ordered list of heights of the vertices along \vec{u} . Then

$$D(\text{EC}_{\vec{u},I}, \text{EC}_{\vec{u},I^*}) = \sqrt{\sum_{i=1}^{n-1} \int_{h_i}^{h_{i+1}} (\chi(C_{\vec{u},h}) - \chi(C_{\vec{u},h}^*))^2 dh}.$$

Since EC is a piecewise constant function that changes only at the heights of vertices, we can rewrite it as,

$$D(\text{EC}_{\vec{u},I}, \text{EC}_{\vec{u},I^*}) = \sqrt{\sum_{i=1}^{n-1} (h_{i+1} - h_i) (\chi(C_{\vec{u},h_i}) - \chi(C_{\vec{u},h_i}^*))^2}.$$

Let, $e = \max\{h_2 - h_1, \dots, h_n - h_{n-1}\}$. Then

$$D(\text{EC}_{\vec{u},I}, \text{EC}_{\vec{u},I^*}) \leq \sqrt{e} \sqrt{\sum_{i=1}^{n-1} (\chi(C_{\vec{u},h_i}) - \chi(C_{\vec{u},h_i}^*))^2}.$$

Since for $\mathbf{x} \in \mathbb{R}^n$, $\|\mathbf{x}\|_2 \leq \|\mathbf{x}\|_1$, we have

$$\begin{aligned} D(\text{EC}_{\vec{u},I}, \text{EC}_{\vec{u},I^*}) &\leq \sqrt{e} \sum_{i=1}^{n-1} |\chi(C_{\vec{u},h_i}) - \chi(C_{\vec{u},h_i}^*)| \\ &= \sqrt{e} \sum_{i=1}^{n-1} \left| \sum_{j=0}^d (-1)^j (\text{Card}(C_{u,h_i}^j) - \text{Card}(C_{u,h_i}^{*j})) \right| \\ &\leq \sqrt{e} \sum_{i=1}^{n-1} \sum_{j=0}^d \left| (-1)^j (\text{Card}(C_{u,h_i}^j) - \text{Card}(C_{u,h_i}^{*j})) \right| \end{aligned}$$

Now for any sub-complex of C , the only cubes that can change are the ones that have \mathbf{v}_0 as a constituent vertex. So, using Lemma 1, we can bound the inner summation by 3^d . Thus we have

$$D(\text{EC}_{\vec{u},I}, \text{EC}_{\vec{u},I^*}) \leq \sqrt{e} 3^d n.$$

Next, we provide a bound for e to complete our proof. Every vertex $\mathbf{v}_0 = (x_1, \dots, x_d)$ has at least d adjacent vertices, say $\{\mathbf{v}_i : i = 1, \dots, d\}$ where $\mathbf{v}_i = (x_1, \dots, x_i \pm 1, \dots, x_d)$. We seek to find an upper bound of the minimum difference between the heights of the vertex \mathbf{v}_0 and any of its adjacent vertices over all possible directions $\vec{u} = (u_1, \dots, u_d) \in \mathbb{S}^{d-1}$. This can be obtained

by solving the following optimization problem:

$$\max_{\vec{u} \in \mathbb{S}^{d-1}} \min_{i \in \{1, 2, \dots, d\}} (|\mathbf{v}_i \cdot \vec{u} - \mathbf{v}_0 \cdot \vec{u}|) = \max_{\vec{u} \in \mathbb{S}^{d-1}} \min_{i \in \{1, 2, \dots, d\}} |u_i|$$

with $\|\vec{u}\| = 1$. The direction vector \vec{u} that maximises this function is the vector with all equal components, i.e., $(1/\sqrt{d}, \dots, 1/\sqrt{d})$. Thus, we obtain an upper bound of e as $1/\sqrt{d}$. ■

Theorem 3. *Let I and I^* be two d -dimensional binary images with vertex set V which differ at k voxels $\mathbf{v}_1, \dots, \mathbf{v}_k$. Then along an arbitrary direction \vec{u} ,*

$$D(\text{EC}_{\vec{u}, I}, \text{EC}_{\vec{u}, I^*}) \leq k3^d n / \sqrt{d}$$

where $n = |V|$.

Proof. From I , we construct a sequence of k images I_0, I_1, \dots, I_k , defined as follows:

$$I_i(\mathbf{v}) = \begin{cases} I^*(\mathbf{v}), & \mathbf{v} = \mathbf{v}_i \\ I_{i-1}(\mathbf{v}), & \text{otherwise} \end{cases}$$

for $i = 1, 2, \dots, k$ and $I_0 = I$. Observe that $I_k = I^*$ and that I_i and I_{i+1} differ by only one voxel for all i from 0 to $k - 1$. Using the triangle inequality of a metric repeatedly and using Theorem 2,

$$\begin{aligned} D(\text{EC}_{\vec{u}, I}, \text{EC}_{\vec{u}, I^*}) &\leq \sum_{i=0}^{k-1} D(\text{EC}_{\vec{u}, I_i}, \text{EC}_{\vec{u}, I_{i+1}}) \\ &\leq \sum_{i=0}^{k-1} 3^d n / \sqrt{d} = k3^d n / \sqrt{d}. \end{aligned}$$

■

Corollary 1. *Let I and I^* be two d -dimensional binary images with vertex set V s.t. they differ at k voxels $\mathbf{v}_1, \dots, \mathbf{v}_k$. Then,*

$$D(\text{ECT}_I, \text{ECT}_{I^*}) \leq k3^d n / \sqrt{d} \times \text{Surface area of } \mathbb{S}^{d-1}$$

where $n = |V|$.

Proof. From theorem 3, the distance between two ECTs, in Eqn 2.5, can be bounded as

$$D(\text{ECT}_I, \text{ECT}_{I^*}) \leq k3^d n / \sqrt{d} \times \int_{\vec{u} \in \mathbb{S}^{d-1}} 1 du$$

■

CHAPTER 5

EXPERIMENTAL RESULTS

5.1 Experimental Results

We test the efficacy of our topological loss function by adding it to the SHAPR model and testing it on a biomedical dataset which have been used in the prior work [8,9].

1. Red Blood Cells(RBC): This is a dataset of 825 3D images obtained from a confocal microscope [22]. These cells are categorized into 9 designated categories: spherocytes, stomatocytes, discocytes, echinocytes, keratocytes, knizocytes, acanthocytes, cell clusters, and multilobates. The dimensionality of each image is $64 \times 64 \times 64$.

These datasets are publicly available.¹ Due to the limited dataset size, we follow the evaluation procedure of Waibel et al. [9]. That is we perform 5-fold cross-validation partitioning the dataset into five folds with a train/validation/test split of 60%/20%/20%. We ensure that each image of a dataset appears in the test split exactly once. We compare three different approaches to determine the improvements of our proposed loss. Namely, the baseline SHAPR [8], SHAPR with the Wasserstein-based loss [9], and finally SHAPR with our WECT-based loss using both the V and E construction. For the baseline SHAPR and the Wasserstein loss based implementation, we use the code made available by Waibel et al. [9].²

¹<https://hmgubox2.helmholtz-muenchen.de/index.php/s/YAds7dA2TcxSDtr>

²https://github.com/aidos-lab/SHAPR_torch

We follow the same training procedure as in Waibel et al. [9], that is, we train all the variants of SHAPR for a maximum of 100 epochs, using early stopping with a patience parameter of 15 epochs. We also perform data augmentation before training by performing random horizontal or vertical flipping as well as 90° rotations with a 33% probability for an augmentation to be applied on a sample. We track our experiments using WANDB [23]. In the testing phase, we apply Otsu’s thresholding [24] to convert our image into a binary image. This binary image is then compared with the ground truth to calculate three metrics from the prior works, namely, IoU error, relative Volume error and relative surface error. We drop the roughness error from the prior works [8,9] as we believe it does not serve as a useful metric to measure the accuracy of the reconstruction. It is defined as the difference between the predicted image and a 3D smoothed Gaussian version of the image. As seen in Figure FC5.1, even the ground truth is rough in nature and will have a large roughness error.

We train the baseline and Wasserstein loss based model using the hyperparameters reported in Waibel et al. [9]. For our WECT-based loss model, we use gradient clipping of threshold value 0.5. The number of directions we consider in evaluating the integral of the distance function is 100 (l in Algorithm 2). Finally, the parameter M or number of steps (Algorithm 3) we take as 30.

Table TC5.1: Performance of different variants of the SHAPR model on the Red blood cells dataset with the best performing algorithm highlighted in **bold**.

IoU Error (\downarrow)		Volume Error (\downarrow)		Surface Error (\downarrow)	
Dataset	RBC	Dataset	RBC	Dataset	RBC
Baseline	0.539	Baseline	0.422	Baseline	0.263
Wasserstein	0.535	Wasserstein	0.511	Wasserstein	0.348
WECT (V)	0.599	WECT (V)	0.454	WECT (V)	0.278
WECT (E)	0.546	WECT (E)	0.453	WECT (E)	0.211

(a)
(b)
(c)

We can see the results of our experiments in Table TC5.1. We observe that on most metrics our WECT-based with (E) construction performs competitively or the best. We also note that our introduction of the (E) construction is crucial as using the (V) construction gives poor results.

We can visualize the outputs of the various methods (Excluding V construction) on the RBC

dataset in Figures [FC5.1](#), [FC5.2](#). Note that in the current reconstruction problem we cannot expect perfect reconstructions since the problem is ill-posed.

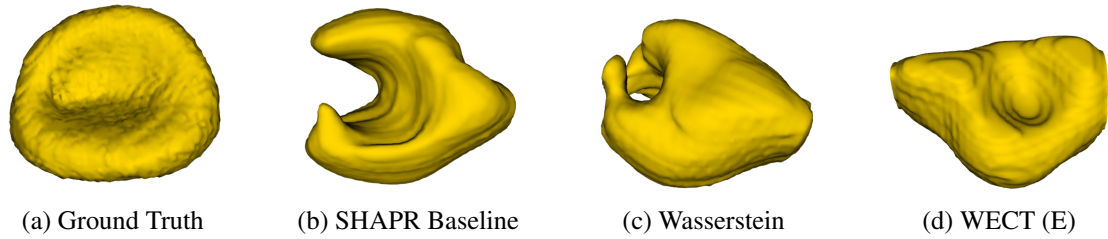


Figure FC5.1: Qualitative results on the RBC dataset. The WECT result is significantly better than the others

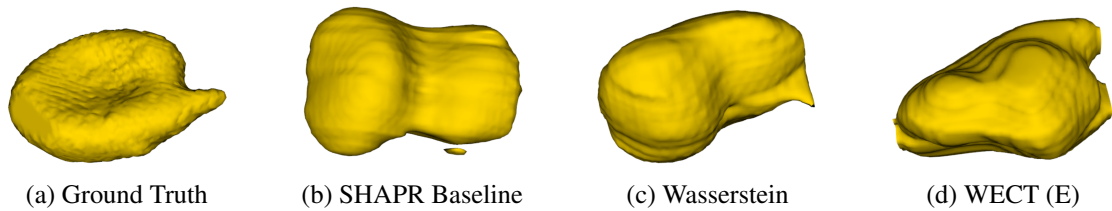


Figure FC5.2: Qualitative results on the RBC dataset. Both the topology losses don't have artifacts unlike the SHAPR baseline

CHAPTER 6

CONCLUSION AND FUTURE WORK

In this thesis, we present a novel WECT-based topological loss function that can be used to aid the training of neural networks for the challenging task of 3D image reconstruction from a single image. We not only show empirical improvement but also discuss some important theoretical properties of our loss and ECT in general. Our WECT-based loss can be used to describe the topological distance between any two images. Our method could thus potentially be employed to aid neural networks in *any* vision task, including image segmentation or 3D image reconstruction from multiple images. It would be interesting to test this hypothesis and observe the performance of our method on different tasks. Another natural extension of our work would be to consider the persistent homology transform (PHT) instead of the ECT. While both are injective, the persistence diagram is more informative than the Euler Curve however at the cost of additional computation. It would be interesting to explore whether this provides any benefit in a practical setting.

Bibliography

- [1] Kalyan Varma Nadimpalli, Amit Chattopadhyay, and Bastian Rieck. Euler characteristic transform based topological loss for reconstructing 3d images from single 2d slices. In *Proceedings of the IEEE/CVF Conference on Computer Vision and Pattern Recognition*, pages 571–579, 2023. Available at [10.48550/arXiv.2303.05286](https://arxiv.org/abs/2303.05286).
- [2] Alexander LeNail. Nn-svg: Publication-ready neural network architecture schematics. *J. Open Source Softw.*, 4(33):747, 2019. Available at <https://doi.org/10.21105/joss.00747>.
- [3] Xian-Feng Han, Hamid Laga, and Mohammed Bennamoun. Image-based 3d object reconstruction: State-of-the-art and trends in the deep learning era. *IEEE transactions on pattern analysis and machine intelligence*, 43(5):1578–1604, 2019. Available at <https://doi.ieeecomputersociety.org/10.1109/TPAMI.2019.2954885>.
- [4] Angel X Chang, Thomas Funkhouser, Leonidas Guibas, Pat Hanrahan, Qixing Huang, Zimo Li, Silvio Savarese, Manolis Savva, Shuran Song, Hao Su, et al. Shapenet: An information-rich 3d model repository. *arXiv preprint arXiv:1512.03012*, 2015. Available at <https://doi.org/10.48550/arXiv.1512.03012>.
- [5] Xingyuan Sun, Jiajun Wu, Xiuming Zhang, Zhoutong Zhang, Chengkai Zhang, Tianfan Xue, Joshua B Tenenbaum, and William T Freeman. Pix3d: Dataset and methods for single-image 3d shape modeling. In *Proceedings of the IEEE Conference on Computer Vision and Pattern Recognition*, pages 2974–2983, 2018. Available at <https://hdl.handle.net/1721.1/132170.2>.

- [6] Nikos Kolotouros, Georgios Pavlakos, and Kostas Daniilidis. Convolutional mesh regression for single-image human shape reconstruction. In *Proceedings of the IEEE/CVF Conference on Computer Vision and Pattern Recognition*, pages 4501–4510, 2019. Available at <https://doi.org/10.48550/arXiv.1905.03244>.
- [7] Katharine Turner, Sayan Mukherjee, and Doug M Boyer. Persistent homology transform for modeling shapes and surfaces. *Information and Inference: A Journal of the IMA*, 3(4):310–344, 2014. Available at <https://doi.org/10.1093/imaiai/iau011>.
- [8] Dominik J. E. Waibel, Niklas Kiermeyer, Scott Atwell, Ario Sadafi, Matthias Meier, and Carsten Marr. SHAPR predicts 3d cell shapes from 2d microscopic images. *iScience*, 25(11):105298, 2022. Available at <https://doi.org/10.1016/j.isci.2022.105298>.
- [9] Dominik J. E. Waibel, Scott Atwell, Matthias Meier, Carsten Marr, and Bastian Rieck. Capturing shape information with multi-scale topological loss terms for 3d reconstruction. In Linwei Wang, Qi Dou, P. Thomas Fletcher, Stefanie Speidel, and Shuo Li, editors, *Medical Image Computing and Computer Assisted Intervention (MICCAI)*, pages 150–159, Cham, Switzerland, 2022. Springer. Available at 10.1007/978-3-031-16440-815.
- [10] Felix Hensel, Michael Moor, and Bastian Rieck. A survey of topological machine learning methods. *Frontiers in Artificial Intelligence*, 4:681108, 2021. Available at <https://doi.org/10.3389/frai.2021.681108>.
- [11] Xiaoling Hu, Yusu Wang, Li Fuxin, Dimitris Samaras, and Chao Chen. Topology-aware segmentation using discrete morse theory. *arXiv preprint arXiv:2103.09992*, 2021. Available at <https://doi.org/10.48550/arXiv.2103.09992>.
- [12] Doruk Oner, Adélie Garin, Mateusz Kozinski, Kathryn Hess Bellwald, and Pascal Fua. Persistent homology with improved locality information for more effective delineation. Technical report, 2022. Available at <https://doi.org/10.48550/arXiv.2110.06295>.
- [13] Fan Wang, Huidong Liu, Dimitris Samaras, and Chao Chen. Topogan: A topology-aware generative adversarial network. In *Computer Vision–ECCV 2020: 16th European Con-*

- ference, Glasgow, UK, August 23–28, 2020, Proceedings, Part III 16*, pages 118–136. Springer, 2020. Available at <https://doi.org/10.1007/978-3-030-58580-88>.
- [14] Dominik J. E. Waibel, Ernst Röell, Bastian Rieck, Raja Giryes, and Carsten Marr. A diffusion model predicts 3d shapes from 2d microscopy images. *arXiv preprint arXiv:2208.14125*, 2022. Available at <https://doi.org/10.48550/arXiv.2208.14125>.
- [15] Herbert Edelsbrunner and John L Harer. *Computational topology: an introduction*. American Mathematical Society, 2022.
- [16] Bastian Rieck, Tristan Yates, Christian Bock, Karsten Borgwardt, Guy Wolf, Nicholas Turk-Browne, and Smita Krishnaswamy. Uncovering the topology of time-varying fMRI data using cubical persistence. *Advances in Neural Information Processing Systems*, 33:6900–6912, 2020. Available at 10.5555/3495724.3496303.
- [17] Madjid Allili, Konstantin Mischaikow, and Allen Tannenbaum. Cubical homology and the topological classification of 2d and 3d imagery. In *Proceedings 2001 international conference on image processing (Cat. No. 01CH37205)*, volume 2, pages 173–176. IEEE, 2001. Available at 10.1109/ICIP.2001.958452.
- [18] Qitong Jiang, Sebastian Kurtek, and Tom Needham. The weighted euler curve transform for shape and image analysis. In *Proceedings of the IEEE/CVF Conference on Computer Vision and Pattern Recognition Workshops*, pages 844–845, 2020. Available at 10.1109/CVPRW50498.2020.00430.
- [19] Justin Curry, Sayan Mukherjee, and Katharine Turner. How many directions determine a shape and other sufficiency results for two topological transforms. *Transactions of the American Mathematical Society, Series B*, 9(32):1006–1043, 2022. Available at <https://doi.org/10.1090/btran/122>.
- [20] David Cohen-Steiner, Herbert Edelsbrunner, and John Harer. Stability of persistence diagrams. In *Proceedings of the twenty-first annual symposium on Computational geometry*, pages 263–271, 2005. Available at <https://doi.org/10.1007/s00454-006-1276-5>.

- [21] Primoz Skraba and Katharine Turner. Wasserstein stability for persistence diagrams. *arXiv preprint arXiv:2006.16824*, 2020. Available at <https://doi.org/10.48550/arXiv.2006.16824>.
- [22] Greta Simionato, Konrad Hinkelmann, Revaz Chachanidze, Paola Bianchi, Elisa Fermo, Richard van Wijk, Marc Leonetti, Christian Wagner, Lars Kaestner, and Stephan Quint. Red blood cell phenotyping from 3d confocal images using artificial neural networks. *PLoS Computational Biology*, 17(5):e1008934, 2021. Available at <https://doi.org/10.1371/journal.pcbi.1008934>.
- [23] Lukas Biewald. Experiment tracking with weights and biases, 2020. Software available from <https://www.wandb.com/>.
- [24] Nobuyuki Otsu. A threshold selection method from gray-level histograms. *IEEE Transactions on Systems, Man, and Cybernetics*, 9(1):62–66, 1979. Available at doi: <https://doi.org/10.1109/TSMC.1979.4310076>.